Evaluating the freeze-thaw phenomenon in sandwich-structured composites via numerical simulations and infrared thermography

Stefano Sfarra [1*, 2], Blanca Tejedor [3], Stefano Perilli [1], Ricardo M.S.F. Almeida [4, 5], *and* Eva Barreira [4]

[1] Department of Industrial and Information Engineering and Economics (DIIIE), University of L'Aquila, Piazzale E. Pontieri 1, I-67100, Monteluco di Roio – L'Aquila (AQ), Italy
[2] Tomsk Polytechnic University, Lenin Av., 7, 634050, Tomsk, Russia
[3] Department of Project and Construction Engineering – Group of Construction Research and Innovation (GRIC), Universitat Politècnica de Catalunya – UPC, C/Colom 11, Edifici TR5, 08222 Terrassa (Barcelona), Spain
[4] CONSTRUCT – LFC, Faculty of Engineering (FEUP), University of Porto, Rua Dr. Roberto Frias s/n, 4200-465 Porto, Portugal
[5] Polytechnic Institute of Viseu, School of Technology and Management, Department of Civil Engineering, Campus Politécnico de Repeses, 3504-510 Viseu, Portugal

[*]corresponding email's author: stefano.sfarra@univaq.it

Abstract: The water ingress phenomenon in sandwich-structured composites used in the aerospace/aeronautical sector is a current issue. This type of defect can cause in the course of time several other defects at the boundary, such as corrosions, deformations, detachments, *etc*. In fact, water may change its state of physical matter going towards the freeze-thaw cycle caused by the atmosphere re-entry of, *e.g.*, space probes. In this work, the alveoli of a composite laminate have been filled with water, which was initially transformed into ice. By taking into account the known quantity of water, the freeze-thaw cycle was simulated by Comsol Multiphysics® software, reproducing exactly the shape of the sandwich as well as the real conditions in which it was subsequently subjected in a climatic chamber. The experimental part consisted of monitoring the front side of the specimen by means of a thermal camera operating into the long-wave (LW) infrared spectrum, and by setting both the temperature and the relative humidity of the test chamber according to the values imposed during the numerical simulation step. It was found that the numerical and experimental temperature trends are in good agreement with each other since the model was built by following a physico-chemical point-of-view. It was also seen that the application of the independent component thermography (ICT) technique was able both to retrieve the positions of the defects (*i.e.*, the water inclusions) and to characterize the defects in which a detachment (fabricated between the fibres and the resin) is present; the latter was realized above an inclusion caused by the water ingress. To the best of our knowledge, this is the first time that ICT is applied to satisfy this purpose.

Keywords: Infrared thermography; Heat transfer; Climatic chamber; Composite materials; Image processing; Numerical simulation; Freeze-thaw phenomenon; Water ingress.

1. Introduction

Water ingress in aircraft honeycomb sandwich structures is an ongoing issue that has attracted significant attention from aircraft operators, maintenance depots and the research community. Water ingress can lead to skin-to-core bonding degradation, affecting structural integrity [1]. As the mechanism of water ingress induced bonding degradation is not well-understood yet [2], it usually is required that this liquid in the honeycomb core be removed to avoid bonding degradation. A process to remove water from the alveoli

of the honeycomb involves drilling holes in one side of the skins, puncturing holes in the honeycomb cell walls, removing water through heat drying, and finally proceed to install a bonded repair patch over the drilled area [3]. Unfortunately, the original paths for water ingress are not resolved and there is a potential for the introduction of new water ingress paths from the drain holes.

The water ingress problem in aviation structures has been studied by several authors. In the following brief review, we will focalize the attention on the infrared thermography (IRT) method that is able to provide information concerning such open problem. This is because in the present research work the authors combined its potentialities to the advantages provided by an advanced numerical simulation performed in Comsol Multiphysics® environment.

In Anon [4] is reported that the European airliner manufacturer Airbus Industries of Toulouse, France, developed in 1994 a thermographic inspection technique for detecting possible water ingress in composite sandwich structures. By considering the research, Airbus recommended that all operators of their aircrafts should adopt the new method as the standard inspection measure for such parts.

Vavilov and Nesteruk studied the hidden water in aviation honeycomb panels by means of IRT method. In fact, water has a high thermal capacity that slows temperature changes. The manuscripts described quantitative aspects of the water detection problem. In particular, simulation results were obtained by analysing a one-dimensional model of a multi-layer plate where the ice-to-water phase transformation took place. Experimental results inherent to Russian airplanes were presented, too [5–6].

Crawley [7] underlined the fact that moisture ingress into sandwich structures is believed to occur by one of two methods, via diffusion through the bulk adhesive layer or by wicking along the adhesive-adherend interface. Once the moisture gains access to the honeycomb cells, it leads to corrosion, bond degradation and eventually failure of the component. Both for IRT and conventional NDT techniques, the question still remains as to the exact nature of the indications and whether or not the component remains serviceable. To make this connection, testing has been performed on a series of CF-18 honeycomb rudders in an attempt to develop a correlation between the degraded mechanical properties and various types of NDT inspection indications, providing for a better method for assessments of serviceability of composite honeycomb panels.

In the work developed by Tang *et al.* [8], a probability of detection (POD) assessment, using the MIL-HDBK-1823 Non-destructive Evaluation System Reliability Assessment methodologies, was carried out to quantitatively assess the capability of the Royal Military College (RMC) Neutron Radiology System's (NRS) for detecting water inside CF188 Flight Control Surfaces (FCS). POD curves generated from the reliability testing results demonstrated that the RMC NRS has a water detection reliability of 6.85 /μL for its neutron

radiography system, and 18.23 /μL for its neutron radioscopy system. Additional tests by using the Canadian Forces (CF) X-radiography and IRT methods completed the study.

Lai *et al.* reported the results of a durability study of the effects of exposing externally-bonded CFRP-concrete beams to three elevated water temperatures. The effects of the heated water environments on the adhesive bonding layer between the CFRP and concrete beams were evaluated by quantifying: (1) the changes of delaminations within the adhesive bonding layer, (2) the changes in resistance to direct shear force, and (3) the changes of failure mode distribution. Before the exposure, the condition of the adhesive bonding layer was inspected by IRT. After the exposure, the deterioration of the same bonding layer and failure mode distributions were measured by analysing the visual photos on the failed CFRP strips. The failure modes were found to be affected largely by the combined effect of elevated temperature and moisture ingress [9].

An integrated use among holographic interferometry (HI) and IRT for the inspection of honeycomb sandwich structures with fabricated defects has been discussed in [10]. The main advantages and limitations of both techniques are enumerated and discussed.

Válek *et al.* studied in a field-scale experiment the potential benefit of several non-destructive testing methods to assess the water damage in building stones. Three testing walls made of fired clay brick, sandstone, and spongilite were flooded and their drying behaviour monitored using IRT, complex resistivity, ground penetrating radar, and ultrasonics. The results were compared to the average moisture content determined by gravimetric analysis of the specimens. Qualitatively, the results of the different NDT methods matched well; the same cannot be said from a quantitative point-of-view because a scattering phenomenon was observed [11].

Zeng *et al.* underlined the fact that in aerospace applications, water or oil may ingress in the honeycomb structure and it is important to detect what kind of liquid ingression it is. With the aim to explore this field of research, a 20 /mm thick steel plate was milled with eight circular holes at the back side, and then each hole was filled with different materials: water, oil, air and wax. A special experimental setup was used, while the theoretical model of temperature evolution with time was constructed; the data processing of embedded material filled in steel holes was deduced based on the theoretical model. The air hole was used as a reference. Nine different flash power levels, which changed from full scale power level to one ninth linearly, were used to simulate different noise levels. The calculation results indicate that thermal wave imaging is a potential technology to test the thermal effusivity of an unknown material when it is embedded in a known material [12–13].

The mechanism of pulsed thermography (PT) for water detection in aviation composite panels was studied by numerical simulations and experiments in [14]. The authors presented a new 3D heat conduction model of water detection in honeycomb panels. The relationships between information parameters and water were analysed for three testing modes in which both the maximum temperature difference and maximum contrast were non-linear functions of the water height, increasing with higher water height. It was found that both water ingress and glue have a similar influence on the surface temperature and, therefore, they cannot be distinguished by the temperature difference curve or the maximum temperature difference information. The authors said that the results obtained can provide technical support for water detection and evaluation of aviation honeycomb structures by PT.

Also Ibarra-Castanedo *et al.* studied the water ingress effect in honeycomb sandwich panels [15]. They applied the passive IRT approach using a high-resolution thermal imaging camera. In particular, the testing specimens were produced from unserviceable parts from military aircraft. In order to simulate atmospheric conditions during landing, selected core areas were filled with measured quantities of water and then frozen in a cold chamber. The specimens were then removed from the chamber and monitored for over 20 minutes as they warm up using a cooled high-resolution infrared camera. Results have shown that detection and quantification of water ingress on honeycomb sandwich structures by passive thermography is possible by using a high-definition mid-wave infrared camera for volumes of water as low as 0.2 /ml and from a distance as far as 20 /m from the target.

In the study conducted by Chen *et al.*, honeycomb specimens with glass fiber and aluminium skin were injected by means of different kinds of liquids: water and oil. PT was adopted and a recognition method was then proposed to first get the reference curve by linear fitting the beginning of the logarithmic curve. Consequently, an algorithm based on the thermal contrast between liquid and reference was used to recognize what kind of fluid was detected, by calculating the respective thermal properties. Finite element (FE) simulations were used to support the results [16]. An improved version of the idea was published in [17].

The use of IRT on glass reinforced plastic (GRP) wind turbine blades assessment was presented by Avdelidis *et al.* [18]. Interestingly, the development of an autonomous, novel and lightmass multi-axis scanning system deploying *in situ* thermography NDT is also shown.

It was found that a Church (12^{th}–13^{th} Century) located at Talamanca de Jarama, Madrid, Spain, shows a complex building history due to various constructions and remodelling stages, which affected water ingress in the walls [19]. Moisture distribution of selected areas of the walls was monitored. Sensing techniques included wireless sensor networks, electrical resistance tomography, IRT and portable moisture meters.

Outdoors, indoors and internal temperature and relative humidity of the walls at different depths were monitored. A comparative study of IRT and electrical resistance tomography to characterize the thermal and hygrometric behaviour of the most affected wall is also included in the discussion of the results. Also in [20], the effect of wetting and drying in building materials was evaluated using IRT and portable moisture meters.

The correlation among infrared imaging and photovoltaic performance was at the basis of the research conducted by Adams *et al.* concerning the water ingress in encapsulated inverted solar cells [21]. Through comparison of electroluminescence imaging, lock-in thermography, and photoluminescence mapping, the device performance was correlated with the loss of effective cell area and it was shown that the reaction of water at the hole extraction/active layer interface was likely to be the dominant cause for long-term device failure. The findings of this study inform strategies for predicting lifetimes of organic solar cells and modules based on local in situ tracking of moisture-induced device performance loss using IR imaging.

Saarimäki and Laatikainen studied the fact that the number of penetrated water-induced failures in composite sandwich panels is rising, therefore penetrated water in the composite structures operating in arctic conditions was a research activity developed in Finland. The thermographic inspection method has shown to be the only method that detects small amounts of penetrated water from large areas without removing aircraft composite parts from the aircraft [22].

Isakov proposed a novel approach to detect water ingress along rivets and screws or other discontinuities. The approach was implemented through the generation of a local vacuum. The evaporation process consumed heat energy from the surroundings, causing a decrease in local temperature that was detected by IRT. Using water droplets of different sizes, it was shown that the measured result is a complex phenomenon. Although the exact estimation of water ingress volume did not seem to be feasible, the method has proven to be reliable and it was several orders of magnitude more sensitive in comparison with results reported earlier [23].

In [24], it is remark that for thermographic NDT inspection is difficult to discriminate, both theoretically and experimentally, between the presence of water and epoxy trapped in honeycomb cells, by analysing only the surface temperature patterns. It has been demonstrated that water trapped in honeycomb cells can be reliably detected by an increase in effusivity starting from the inflection time. This process is referred to as the “concept of apparent effusivity”. Similar researches supported with numerical results have been conducted in [25–26]. In particular, the authors focused the attention on the thickness of the water layer affecting the surface temperature anomalies and times of their appearance in active one-sided thermal tests.

Bora *et al.* applied an imaging technique for mapping water ingress in photovoltaic module packaging materials that discriminates high versus low water content regions based on the differential absorption of infrared light corresponding to the water absorption band. The principle of increased absorbance upon water ingress was demonstrated using transmission spectroscopy in encapsulant laminates, and an imaging approach was shown to identify moisture ingress in laminate samples [27].

Interestingly, neural networks were used in IRT field to classify defects, such as air, oil, and water, which can degrade material performance. Finite element (FE) methods and experiments were adopted to simulate air, water, and oil ingress. Quantitative comparisons showed that the model using coefficients as features performed better than the one using raw data. In particular, a long short term memory recurrent neural network (LSTM-RNN) model, which automatically classifies common defects occurring in honeycomb materials, was used [28–29].

Lastly, lock-in thermography (LT) was employed to inspect water ingress in aircraft honeycomb structures, and an investigation into the effect of water content on the quantitative estimation was carried out in [30]. Here, three LT algorithms, namely, fast Fourier transform (FFT), Harmonic approximation, and principle component analysis (PCA) were discussed for quantitative assessment and their performance was compared in terms of signal-to-noise-ratio (SNR).

In this paper, it is assessed if the use of the recently introduced independent component thermography (ICT) [31–32] is a suitable technique to detect the phase change (from solid to liquid) of low volumes of water present into honeycomb cells. In this work, water passed from the solid aggregation state to the liquid aggregation state thanks to the use of a couple of climatic chambers. In the second climatic chamber, a thermal camera was installed in order to record thermograms in the course of time. The potentialities of the ICT technique were explored on a set of thermograms influenced by the changing of the environmental conditions previously studied by a numerical model.

A controlled injection of fluid by filling some alveoli of the honeycomb core anticipated the experimental analyses that were conducted by IRT method. In this work, the drilling procedure was used to simulate the water ingress effect in four different areas of a sandwich panel, one of which located beneath a fabricated detachment. Therefore, we are studying the first entry of water and not a possible and subsequent re-entry.

Through modelling, the following assessments were possible: a) correct quantity of fluid to be injected into every alveolus, b) time necessary to obtain a change in the state of aggregation of the fluid from solid to liquid, and c) assessment of the change of aggregation state by monitoring the temperature evolution throughout the time frame.

The experimental research allowed verifying the goodness of the numerical model, as well as the presence of superficial detachments between the core and external layers. The experimental validation was conducted via IRT.

The paper is organized as follows: at first, the information concerning test sample and the fabrication of defects are introduced, secondly, the advanced numerical model is described, thirdly, the complex physics of the Comsol model along with the mechanisms of the thermal properties at the base of the freeze-thaw phenomenon is presented, fourthly, the description of the experimental test is added to the discussion, fifthly, the *results and discussion* section is presented, sixthly, the analyses of the defects by means of the ICT technique is added to the discussion, and lastly, the conclusions are provided to the readers.

2. Description of the defective sandwich structure (general and detailed view)

The specimen analysed is a typical composite used for coatings belonging to structural components [33–34]. Given the complexity and cost of production, this technology is used for aeronautical parts that need lightness and strength properties. In fact, the use of these types of panels is generally preferred for high-performance aeronautical components. The material is structurally strong, thin, light (considerable volume / mass ratio) and optically translucent, *i.e.*, the inner layers are visible. The specimen is part of the sandwich composites category. It was fabricated by arranging two outer layers of fiberglass, while the inner layer is an aluminium honeycomb core (MIL-C-7438) having the geometric features of 1/8`` × 0.015 × 6.1 /mm.

The test involved the analysis of the thermal response of the specimen subjected to a thermal cycle, with controlled thermo-hygrometric conditions, to evaluate the effects of the water ingress in some alveoli (*i.e.*, the honeycomb cells) of the sandwich itself.

The specimen was assembled by gluing three main layers for a total thickness of 9.53 /mm. Every layer of adhesive interposed between the honeycomb and the covering skins has a thickness of 1.715 /mm, while every alveolus of the aluminium layer is characterized by a volume of 62.35 /mm^3. Regarding the specimen fabrication, it was necessary to use a rigid mold whose geometric characteristics reproduced the desired shape in negative. In the case here analysed, the mold had a flat, smooth and regular surface. The assembly of the specimen involved a layer of release agent that allowed the removal of sacrificial layers without damaging the surface at the end of the construction phase. The release agent forms a transparent, thin film that does not alter the final geometry but slightly attenuates the surface roughness of the final layer. Therefore, the behaviour is similar to a typical colour paint surface. After the addition and drying of the release agent, an adhesive layer was applied; in fact, it is a necessary step at the beginning of the fabrication of the composite. On this layer, fiberglass and resin sheets were alternated each other. The last layer was the

adhesive; this, to make the honeycomb core in aluminium integral with the adhesive itself. After this layer was made, the resin necessary for the adhesion between the aluminium and the upper surface layer was sprinkled by means of a roller. It too, similarly to the base layer, is made up of several fiberglass layers.

In Fig. 1, the specimen is shown. In particular, Fig. 1a shows the front view, while Fig. 1b shows the rear view.

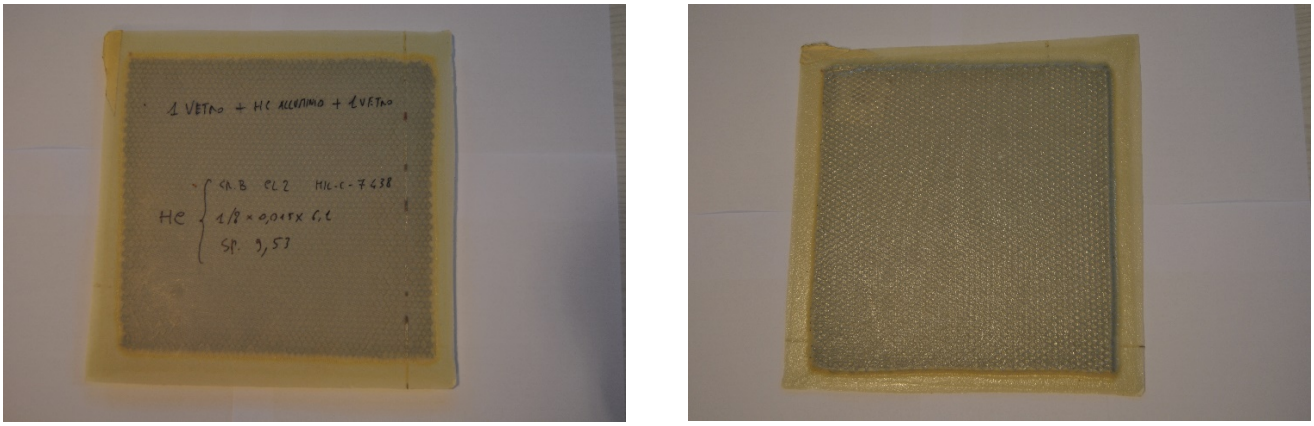

a) b)

Fig. 1 – Specimen: a) front side, and b) rear side.

In order to study the effects of thermal responses dependent on a fabricated detachment realized between the layers, a small area of the specimen was identified for which the resin between the aluminium and the last layer is not present. A Mylar sheet (*i.e.*, a biaxially-oriented polyethylene terephthalate) was added during fabrication as usual when detachments need to be simulated [35–36]. The area without bonding has the extension of the red rectangle shown in Fig. 2.

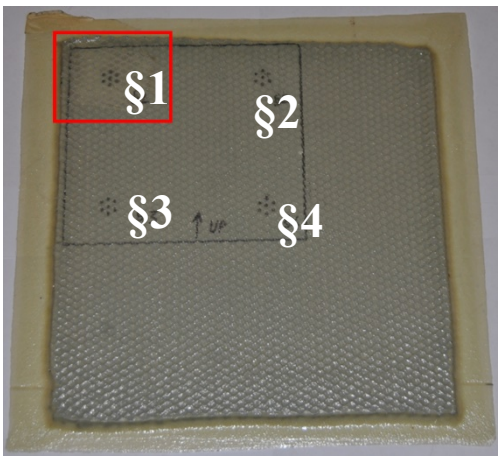

Fig. 2 – Specimen: the fabricated detachment is included in the red rectangle.

Looking at the final product, the external surfaces have a different aspect both to the view and to the touch. The difference is attributable to the technology used to fabricate the product. In fact, the mold consisted of a flat surface having a low roughness. This ensures that one of the two larger surfaces of the specimen will be perfectly flat. Concerning the gluing of the final layer, the use of the roller allowed to avoid the penetration of the resin inside the alveoli. The alternate layers of fibre and matrix (which constitute the last layer) not being in contact with a continuous support surface, characterize the typical finishing surface that is not perfectly flat locally. This is because the fibres that make up the final layers are only laid on the contours of the honeycomb cells, while the entire remaining area is devoid of a physical support.

The lack of rigidity along the plan, typical of reinforcements during the fabrication phase, gives to the specimen the characteristic locally corrugated profile. For this reason, the specimen has two surfaces that appear – the first – perfectly flat and regular, and – the second – globally flat but locally wavy.

The specimen, after the complete drying of the resin, can be considered structurally very robust. The honeycomb has the role of keeping equidistant the surface layers allowing the transfer of the efforts directed orthogonally to the skins. It is evident that a possible displacement and / or deformation of the honeycomb changes the structure of the specimen itself. A further change may occur due to an unexpected detachment of the parts constituting the composite. The detachment – in particular, if it originates from an edge of the specimen – makes possible inclusions from outside. If this eventuality occurs, the inner layers of the composite may come into contact with water vapor or moisture.

The worst case occurs with fluid penetration (in the state of liquid aggregation) inside the honeycomb. The possible presence of a fluid inside the core may involve the problem of chemical attack of the fibre-matrix and/or resin. This defect may appear several months after the event of water ingress and, therefore, it was not taken into account neither during the building of the numerical model nor during the discussion of the experimental results. The contamination is evident if the fluid penetrates the structure reacting with the materials being analysed. This may change its physical and chemical characteristics. Generally, the penetration of the fluid occurs through the external surface of the specimen, or through a discontinuity present on the skin. It was followed during the execution of the defects shown in Fig. 2. However, this mechanism is not the only one that may involve the damage under evaluation [37].

In order to study the behaviour of the fluid (*i.e.*, water) in the alveoli, it was necessary to drill holes (diameter: 0.8 /mm) on one of the two superficial skins constituting the specimen. This choice was taken to reduce the problems linked to both the lack of material (as a result of the drilling process), and to the small size of each cell.

It was decided to perform a drilling procedure only on the completely flat surface. The region of interest (ROI) is equal to 103 × 94 /mm^2, and four zones (§1, §2, §3, §4) (Fig. 2) useful to perform the water ingress procedure were selected. They are positioned along the main diagonals of the ROI.

In order to evaluate the effect of the fluid inlet (water ingress) after the change of state aggregation [38], given the low volume of a single cell equal to 62.35 /mm^3, it was decided to study the behaviour for each cell group marked with the symbol §. In general, each area has a total of 7 cells (*i.e.*, alveoli) adjacent to each other. This, with the aim of evaluating a sufficiently significant content of the fluid in the solid aggregation state. In this way, the area linked to the presence of fluid becomes equal to 72.74 /mm^2, while the volume of fluid injected was 436.48 /mm^3. This happens for each § zone.

In particular, the holes were designed to insert a hypodermic needle (Gauge 21), which was necessary to fill every alveolus. The choice of the calibre was carried out by considering two aspects: a) the first aimed at minimizing the diameter of the hole in order to modify slightly the conformation of the specimen, and b) the second aimed at technological difficulties in drilling a very resistant layer using a sufficiently robust tip for microelectronics.

3. Construction of the numerical model

The geometric model added into Comsol Multiphysics® software is constituted by three layers forming the sandwich panel where the core is the most complicated geometric structure to be reproduced. The latter, being regular in the direction of thickness, was exactly duplicated in the plan through Draftsight® software. Subsequently, it was imported into Comsol Multiphysics® and thanks to the *extrude* command, the desired 3D geometry was obtained. Therefore, the surface layers which represent the upper and lower bases of the specimen were built. In the model, every single layer making up the specimen was added, although only the thermophysical (*i.e.*, not the structural) parameters were included in the input data. The goal of the analysis does not require any verification of the structural properties of the core, of the resin, and of the fibres making up the surface layers. This allowed a lower computational cost, compared to an energetically coupled analysis among thermodynamic and structural behaviour.

This strategy was possible because the specimen – in the laboratory tests – was not structurally loaded. Therefore the structural module was not used in the numerical model and the possible micro-deformations of the alveoli due to the increase in volume from the passage *liquid* → *solid* were not taken into account. However, this phenomenon was not detectable as the increasing effects of the local fluid pressure that occurs as a result of the volumetric expansion in the change of state of aggregation, operated by the walls of the cells that contrast the natural increase in volume, does not occur due to the unmodifiable nature of the alveoli themselves.

On the one hand, the internal local pressure of every alveolus, filled with fluid having a state of solid aggregation, does not increase to the point that the thermodynamic parameters can be modified. On the other hand, the model is computationally more efficient.

The use of the numerical model for the prediction of the thermal response is, therefore, perfectly reasonable to the type of experiment implemented in the laboratory. Following the construction of the geometric model, the mesh of every component was implemented. Given the small thickness of the components (*e.g.*, the alveoli of the core have a thickness of the order of one hundredth of a millimetre), to reduce the computational cost only a small area of the specimen was analyzed (~ a quarter of the extension of the entire specimen). This area, for completeness of the model, also contains a fabricated detachment. Due to the regularity in the direction of the core thickness, a swept mesh was used. This was possible both for the geometric regularity and the preferential orientation of the heat flow that is mainly directed along the thickness. As regards the surface coating (*i.e.*, the skins), a tetrahedral mesh including parameters (*i.e.*, a fine mesh) was needed.

Particular attention was paid to assigning the continuity of the nodal elements at the interface areas. The contacts between the components were managed with appropriate boundary conditions (*Identity Boundary Paid*) typical of the continuity of bonded materials. To avoid the *silly matrix* formations and the problems that would follow due to the inversion in the matrix calculation, the detached area was treated by considering it not as a discontinuity. This area is numerically described as a continuity between two solid materials with an interposed Mylar layer. Even if the areas are in contact, they are not adherent; for this reason, it was reasonable to think that instead of the layer of adhesive there was a layer of Mylar between the elements. In Figs. 3a-d, a) the partial area of the specimen subjected to the meshing, b) the general mesh, c) a detail of the honeycomb, and d) the area subjected to the detachment, are reported, respectively.

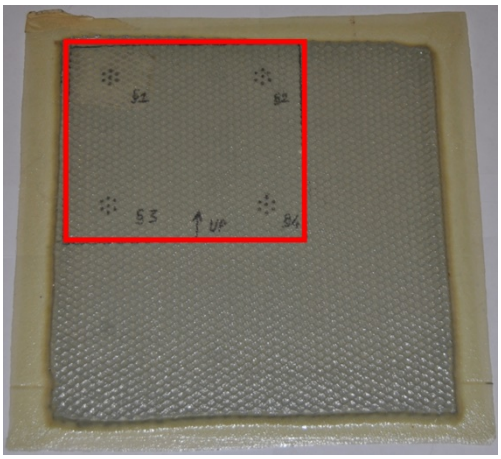

(a)

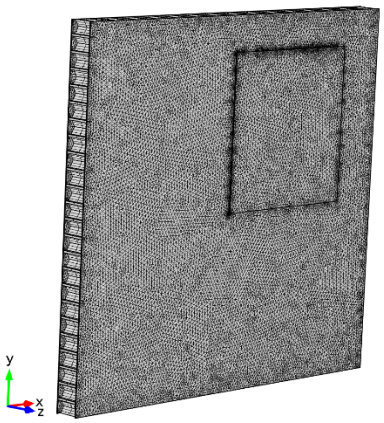

(b)

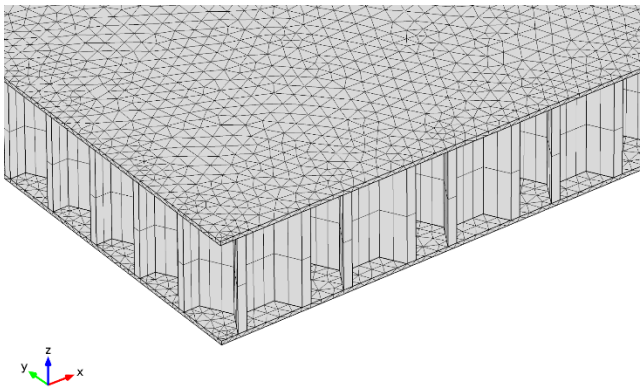

(c)

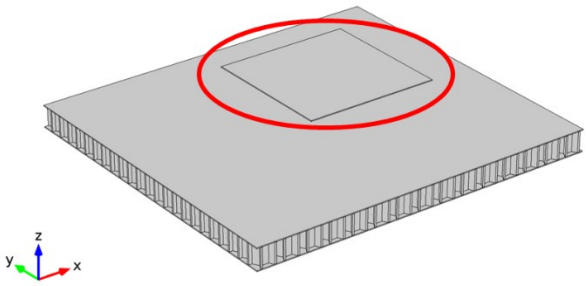

(d)

Fig. 3 – Specimen: (a) Partial area subjected to meshing, (b) the general mesh, (c) the detail of the honeycomb, and (d) the detachment area (marked in red).

In order to allow the penetration of fluid at the state of liquid aggregation, the alveoli were filled by considering the volume of water instead of the volume of air. To achieve the distribution of the volumes in the alveoli, the *union* technique was used instead of the *assembly* technique.

The numerical model does not need holes for the water ingress, as the filling procedure takes place by defining the volume of the corresponding material. For this reason, the holes in the numerical model are not shown.

Tab. 1 summarizes the main materials used to build the sandwich panel, along with the respective thermal properties included in the Comsol Multiphysics® numerical model.

Material	**Density** /kg m^{-3}	**Thermal conductivity** /W m^{-1} K^{-1}	**Specific heat at constant pressure** /J kg^{-1} K^{-1}	**Emissivity**
Honeycomb Aluminium 5052 [39]	2680 [40]	138 [40]	880 [40]	0.09 [41]
Fibreglass panel [42]	2550 [42]	1.2 – 1.35 [42]	800 [42]	0.75 [43]
Resin Permabond® ET538 [44]	1130 [45]	0.55 [44]	1830 [45]	0.95 [46]
Mylar® Polyester Film [47]	1390 [47]	0.1549116 [47]	1172.08 [47]	-
Water (L = liquid) (S = solid)	L at 293.15 /K → 998.21 [48] S at 268.15 /K → 917.5 [49]	L at 293.15 /K → 0.598 [48] S at 268.15 /K → 2.25 [49]	L at 293.15 /K → 0.0041844 [48] S at 268.15 /K → 0.002027 [49]	-

Tab. 1 – Materials used to build the defective sandwich panel along with its main thermal parameters.

4. Physics of the numerical model

The physics used for the analysis conducted in this work was the *Heat Transfer in Solids* and the corresponding equation is as follows (Eq. 1) [50].

$$\rho C_p \frac{\partial T}{\partial t} + \rho C_p \boldsymbol{u} \cdot \nabla T = \nabla \cdot (k \nabla T) + Q \tag{1}$$

where, ρ is the density in /kg m^{-3}, C_p is the specific heat at constant pressure /kJ kg^{-1} K^{-1}, T is the temperature /K, t is the time /s, $\boldsymbol{u}$ is the speed field /m s^{-1}, k is the thermal conductivity /W m^{-1} K^{-1}, and Q is a source / heat sink /J. Eq. 1 analyzes the behaviour of the specimen concerning the parts of the solid material in contact only with the fluid present in the aeriform aggregation state.

As regards the parts of the solid material in contact with the fluid in the state of liquid aggregation, the model is governed by the following Eq. (2):

$$\rho C_p \frac{\partial T}{\partial t} + \rho C_p \boldsymbol{u} \cdot \nabla T = \nabla \cdot (k \nabla T) + Q + Q_{vd} + Q_p \tag{2}$$

where, Q_{vd} indicates a viscous source / heat sink expressed in /J, and Q_p is a point source expressed in /J. For Eq. (2), the density is expressed as:

$$\rho = \theta \rho_{phase1} + (1 - \theta) \rho_{phase2} \tag{3}$$

where, θ is the volume fraction of the fluid present in the cells at the state of solid aggregation, and ρ_{phase1} is the density of the fluid present in the cells at the state of solid aggregation. The term (1–θ) represents the volume fraction of the fluid phase present in the cells at the remaining aggregation state (*i.e.*, liquid), and ρ_{phase2} is the corresponding density.

The specific heat is expressed as:

$$C_p = \frac{1}{\rho}\left(\theta \rho_{phase1} C_{\rho,phase1} + (1 - \theta) \rho_{phase2} C_{\rho,phase2}\right) + L \frac{\partial \alpha_m}{\partial T} \tag{4}$$

where, the terms $C_{\rho,phase1}$ and $C_{\rho,phase2}$ indicate the specific heat at constant pressure for the fluid in the state of solid and liquid aggregation, respectively. In addition, the term L represents the latent heat /J, while α_m is the mass fraction expressed as below:

$$\alpha_m = \frac{1}{2} \frac{(1 - \theta) \rho_{phase2} - \theta \rho_{phase1}}{(1 - \theta) \rho_{phase2} + \theta \rho_{phase1}} \tag{5}$$

It should be noticed that k is expressed as in Eq. (6).

$$k = \theta k_{phase1} + (1 - \theta) k_{phase2} \tag{6}$$

where, k_{phase1} and k_{phase2} are the thermal conductivity of the fluid in the state of solid and liquid aggregation, respectively.

As explained above, the specimen has two external surfaces, nearly parallel. During the thermographic test, the sandwich panel remained in a vertical position; the boundary condition used is shown in Eq. (7).

$$-\boldsymbol{n} \cdot (-k \nabla \mathrm{T}) = h \cdot (T_{ext} - T) \tag{7}$$

where, $-\boldsymbol{n}$ indicates the axis normal to the alveoli of the specimen and entering into them, T_{ext} is the temperature of the external environment where the specimen was installed, T is the instantaneous wall temperature, and h is the convection coefficient.

The convection coefficient is a function of the following parameters: a) characteristic length of the slab subjected to the crossing flow, b) the air pressure, and c) the instantaneous external temperature. Therefore, h can be considered as:

$$h = h_{air}(L, p_{air}, T_{ext}) \quad (8)$$

where, h_{air} represents the natural convection coefficient of the air fluid that laps the surface, p_{air} is the atmospheric pressure /Pa and, finally, L describes the characteristic dimension of the surface of interest /m^2.

The wavy surface is responsible for the reduction of the overall area linked to natural convection. In order to evaluate the behaviour of superficial convection in the area of interest, both surfaces having a predominant vertical and horizontal development along with the respective L and h_{air} exposing their area towards this type of heat transmission, were evaluated.

In Fig. 4 the area of interest surrounded by a red circle is shown. In relation to it, the boundary conditions indicated in Eq. (8) were evaluated individually.

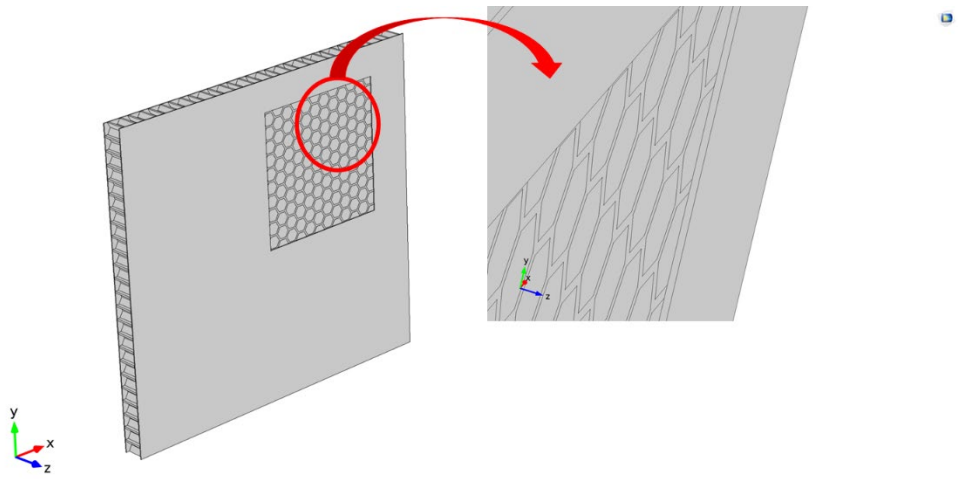

Fig. 4 – The area in which the boundary conditions modelled by Eq. (8) were applied. The boundary conditions were applied to the thickness of the honeycomb in contact with the skin.

Finally, both the *absolute pressure* and the *strain reference temperature* were defined as equal to 1 /atm for the absolute air pressure, and 273.16 /K for the reference temperature related to thermal expansion. The latter is the temperature beyond which the thermal expansion of the fluid begins and also represents the triple point for water.

5. Description of the experimental test

For a sake of clarity to the readers, Fig. 5 shows the specimen with the indication of the seven points per area on which the drilling process was performed.

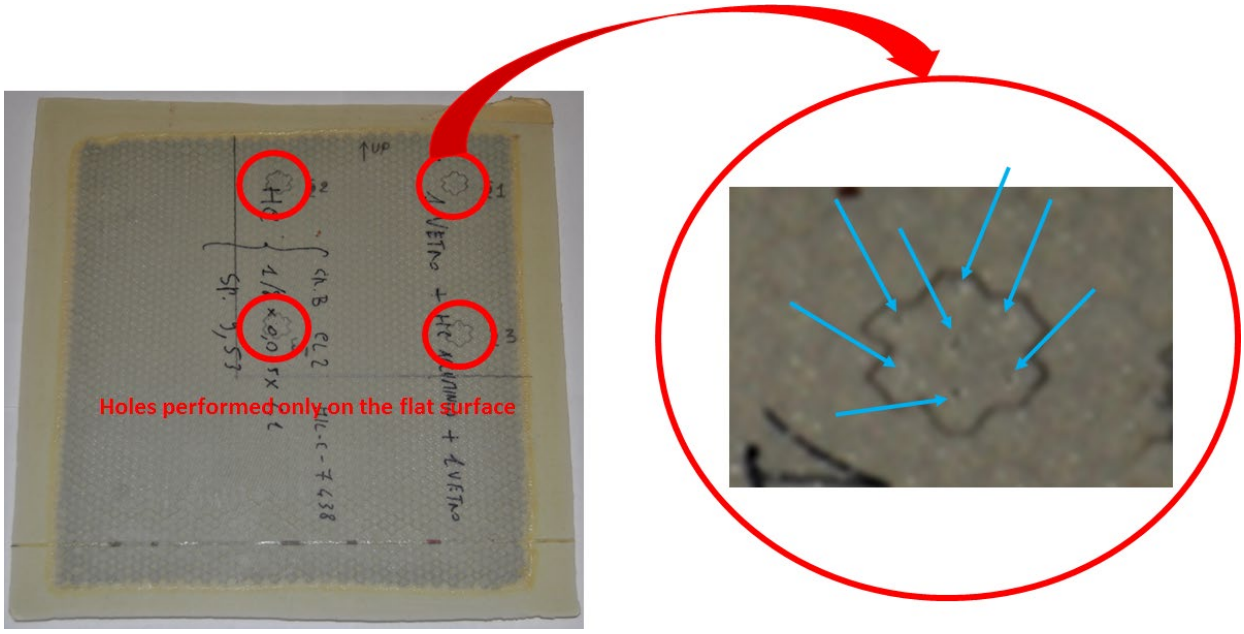

Fig. 5 – Specimen: in red, the § areas (Fig. 2) are indicated while, in blue, the seven holes are pointed out.

Several experimental campaigns took place in the Laboratory of Building Physics of the Faculty of Engineering of the University of Porto – Faculty of Engineering (FEUP). In particular, the specimen was introduced in the first climatic chamber under 253.15 /K and left there for 1 hour (Fig. 6a). Here, the fluid injection procedure took place. Subsequently, the specimen was moved to the second climatic chamber using special pliers with plastic material in order to reduce a possible local thermal disturbance. It should be noted that this climatic chamber had been set at 288.15 /K for at least 2 hours prior to the IRT testing, achieving steady-state conditions and an air volume with similar characteristics at any point in the room. The significant thermal gradient (between the first and second climatic chambers) led the specimen to adapt itself rapidly to the new temperature condition. Nevertheless, this ΔT was considerable high to guarantee enough time to operate the measurement by IRT.

As regards the position of the specimen, a simple structure built with EPS (Fig. 6b) was used to maintain it vertical.

(a) (b)

Fig. 6 – Specimen positioned inside: (a) the first climatic chamber, and (b) the second climatic chamber for the IRT testing.

All the environmental parameters (temperature and humidity), as well as the IR images taken from the wave surface of the specimen, were monitored and recorded over a period of 1 /h, with a data acquisition interval of 10 seconds.

Concerning the measuring equipment, two data loggers HOBO UX100-011 allowed ensuring the inner air temperature of both climatic chambers were in accordance with the boundary conditions stated previously in the simulation. The IRT test was executed with an IR camera operating into the long-wave infrared spectrum [NEC TH9100MR, Avio Technologies Ltd] whose features were the following: resolution of 320×240 pixels, accuracy of ±2/ºC or ±2% reading, FOV of 21.7/º×16.4/º, and thermal sensitivity 0.04/ºC at 30/ºC. The IR camera was positioned on a tripod, at a height of 1 /m above the ground level, a distance of 1.5 /m and an angle of 15/º with respect to the sample surface, to avoid its own reflection onto the lens.

A total of 240 thermograms were post-processed by InfReC Analyzer NS9500 Standard v2.6 [Nippon Avionics Ltd, 2001], applying thermal adjustment and palette of high contrast. With the aim of comparing simulation and experimental outcomes, the matrix of average surface temperature values was also obtained for each thermogram. Later, all matrices were assessed by an algorithm developed in MATLAB® environment based on the Independent Component Thermography (ICT) technique.

6. Results and discussion

The numerical model represents the evolution of the temperature range of the specimen. In particular, the test consisted of evaluating the temperature field, starting from the instant $t = 0$ /s where the specimen was at thermal equilibrium (T = 267 /K). The evolution is centred on the analysis of the behaviour for $t > 0$ /s, by considering the specimen immersed in air (T_{amb} = 288.15 /K, and UR = 50%). The goal of the model was the evaluation of the time frame necessary for the specimen to reach the thermal equilibrium with the

new environment where it was immersed. The latter was numerically considered to be of infinite volume and independent by the presence of the specimen itself.

The model estimated the behaviour of the state transition for the alveoli that originally were filled with water in the state of liquid aggregation, highlighting both the transition temperatures and the overall thermal behaviour of the solid components influenced by the effects of the fluid in the liquid state. In particular, a boundary point probe was inserted in the model as shown in Fig. 7.

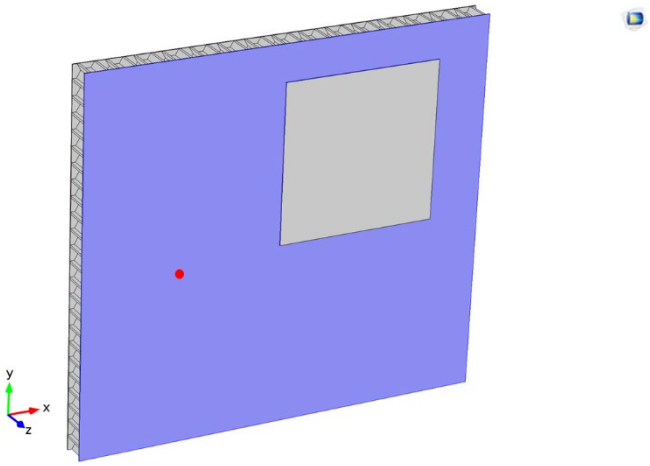

Fig. 7 – Boundary point probe: the position of the virtual temperature sensor is shown in red.

The position shown in Fig. 7 is such that it appears at the center line with respect to the alveoli filled with fluid (*y*-axis), while for the *x*-axis it was in alignment with the vertical cells where the detachment is not present.

This point analyzes an area sufficiently distant from all the possible influences induced on the specimen itself. Therefore, it can be considered as the temperature monitoring point of a defect-free area.

Fig. 8 shows the temperature field of the specimen in a 3D view with thermal equilibrium condition (t = 0 /s).

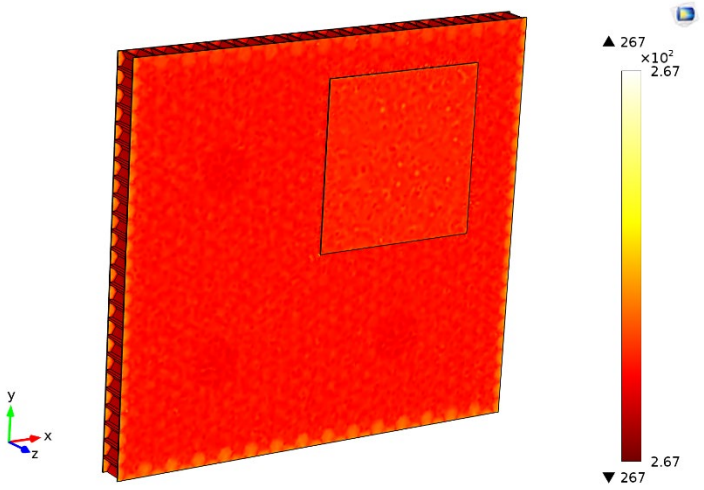

Fig. 8 – 3D view of the temperature field for the specimen at thermal equilibrium (t = 0 /s). The temperature is expressed in /K.

As can be seen in Fig. 8, the temperature field distribution is uniform around the value of 267 /K. It is also possible to notice some chromatic differences on the specimen, which are not directly explained on the colour palette as the extremes have the same value reported both in the entire and normalized notation.

In reality, the calculated range of temperatures varies from 267.04973971154845 /K to 267.056707600999 /K. Given that the comparison of the numerical model is estimated by an experimental test using an acquisition system based on an infrared camera having a thermal sensitivity of ~40 milli-Kelvin, the difference between the previous values can be considered lower to the sensitivity of the instrument; therefore, it is not even reported in the setting of the numerical model.

In Fig. 9, from a) to f), various time instants are shown; here, the trends of the temperature field are evident at intervals of 10 /s up to the first minute of the transition state.

This choice was dictated to highlight the rapid evolution of the temperature range typical of thin objects with low thermal capacity (such as the composite being analysed) in contrast to the water that fills the alveoli having a high thermal capacity and subjected to high external thermal gradients.

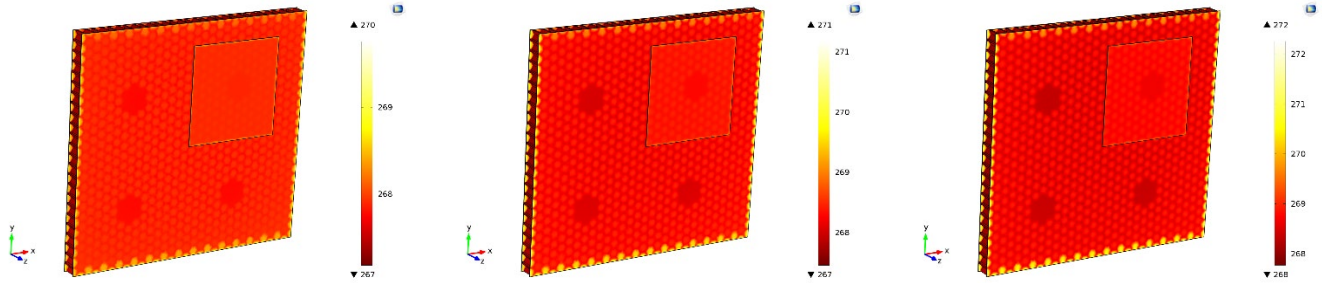

(a) (b) (c)

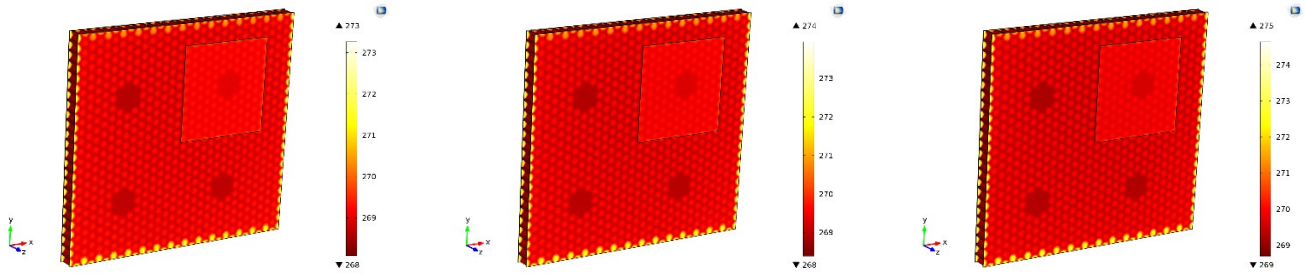

(d) (e) (f)

Fig. 9 – Trend of temperature field in the first minute of transition state: a) 10 /s, b) 20 /s, c) 30 /s, d) 40 /s, e) 50 /s, and f) 60 /s. The temperature is expressed in /K.

In Fig. 9a, at only 10 /s it is possible to notice how the composite rapidly tends to acquire energy in the form of heat, increasing its temperature. On the edge, the effects of the maximum thermal gradient of heating are evident, which occur very quickly thanks to the low thermal capacity of the material and the thin dimensions of the skins. The alveoli filled with water in the state of solid aggregation are barely visible. It is evident that water, having a remarkable thermal capacity, is not quickly affected by the temperature gradient, remaining almost undisturbed for the first 10 /s.

In Fig. 9b), the three alveolar zones §2, §3, §4 filled with water at the state of solid aggregation are more evident, while the fourth zone §1 is still not easely detectable; this is attributable to the detachment between the alveoli and the skin. The Mylar in the detached area causes a thermal insulation that does not allow to clearly visualize the temperature differences between the water and the rest of the material. The specimen has 4 /K of thermal jump within the area analysed.

In Figs. 9 c), d), e) and f), an increase in the internal temperature difference of the specimen is shown and, also, the fourth alveolar zone filled with water in the state of liquid aggregation is now evident.

The Mylar layer at the interface between the alveoli and the skin cannot sufficiently isolate the heat transfer phenomenon and, therefore, this area becomes visible. However, the damping of gradient temperature caused by the detachment is clear in all the figures.

In Figs. 10 a), b), c), d), e), f), g), h), and i) the trends of temperature field from 2 to 10 /min are reported.

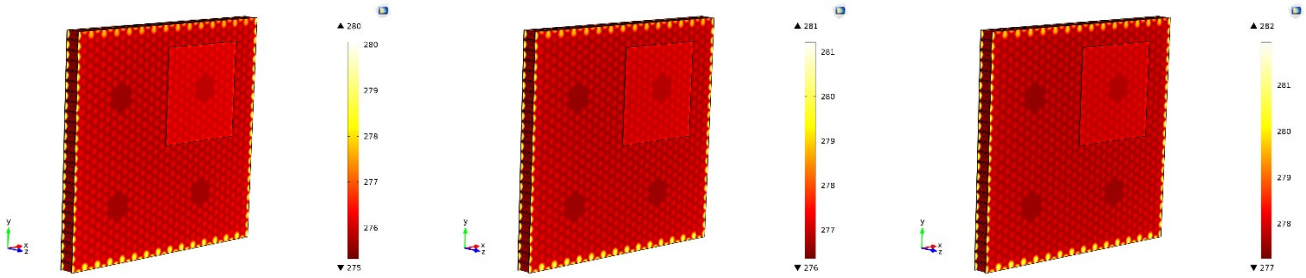

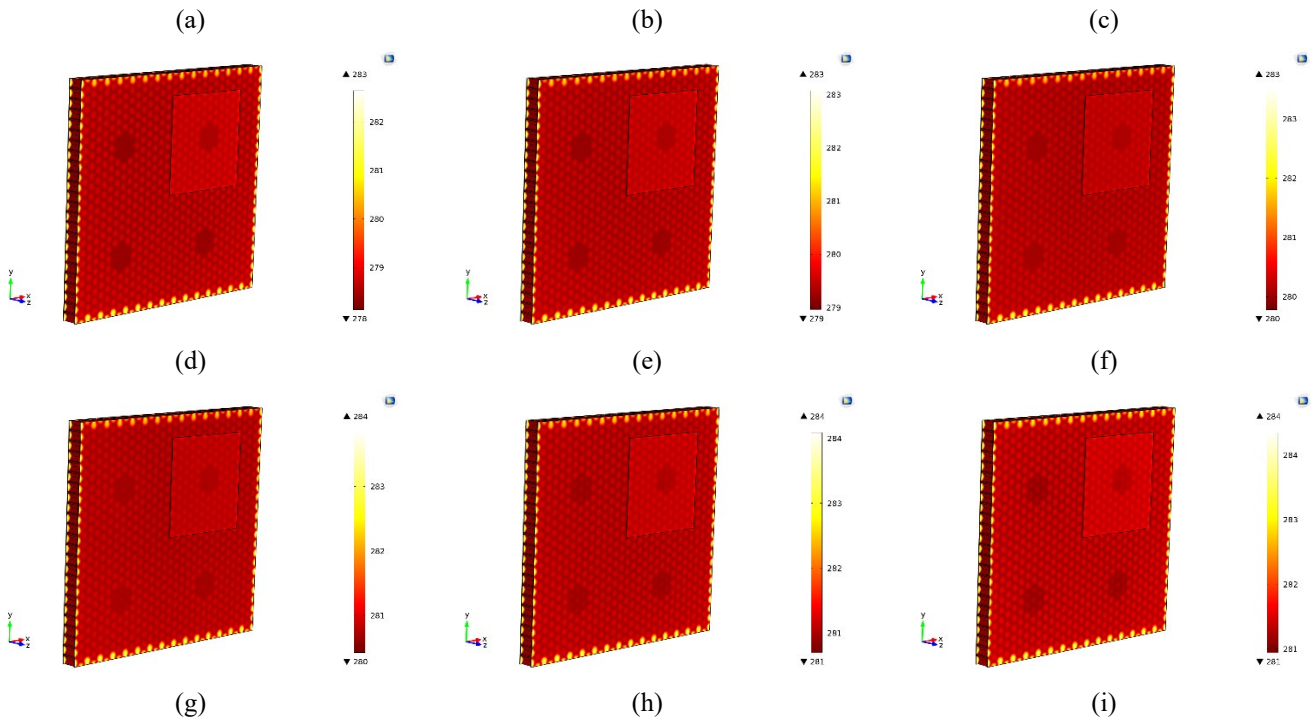

Fig. 10 – Trend of temperature field ranging from 2 to 10 /min of transition state: a) 2 /min, b) 3 /min, c) 4 /min, d) 5 /min, e) 6 /min, f) 7 /min, g) 8 /min, h) 9 /min, and i) 10 /min. The temperature is expressed in /K.

Looking at Figs. 10 it is possible to notice a very similar behaviour throughtout a period from 2 to 10 /min. All the alveoli have undergone the transition of state for a time of 2 /min. The temperature of the areas filled with water in the state of liquid aggregation with respect to the maximum temperature of the specimen remains into an interval of 5 /K for the cases from 2 to 5 /min.

The remaining time instants show the rise in temperature of the fluid, while the maximum temperature value recorded for the rest of the specimen remains constant. Furthermore, the area where the detachment is present still remains at a different temperature compared to the rest of the specimen for all time instants.

In Fig. 11 a), b), c) it is possible to note the trends of the temperature field recorded starting from 20 /min (the time instant of 10 /min is visible in Fig. 10i) with an interval of 10 /min, up to the heat balance. Instead, in Fig. 11 d) it is possible to evaluate an expansion of the alveolar areas filled with fluid in conditions of thermal equilibrium.

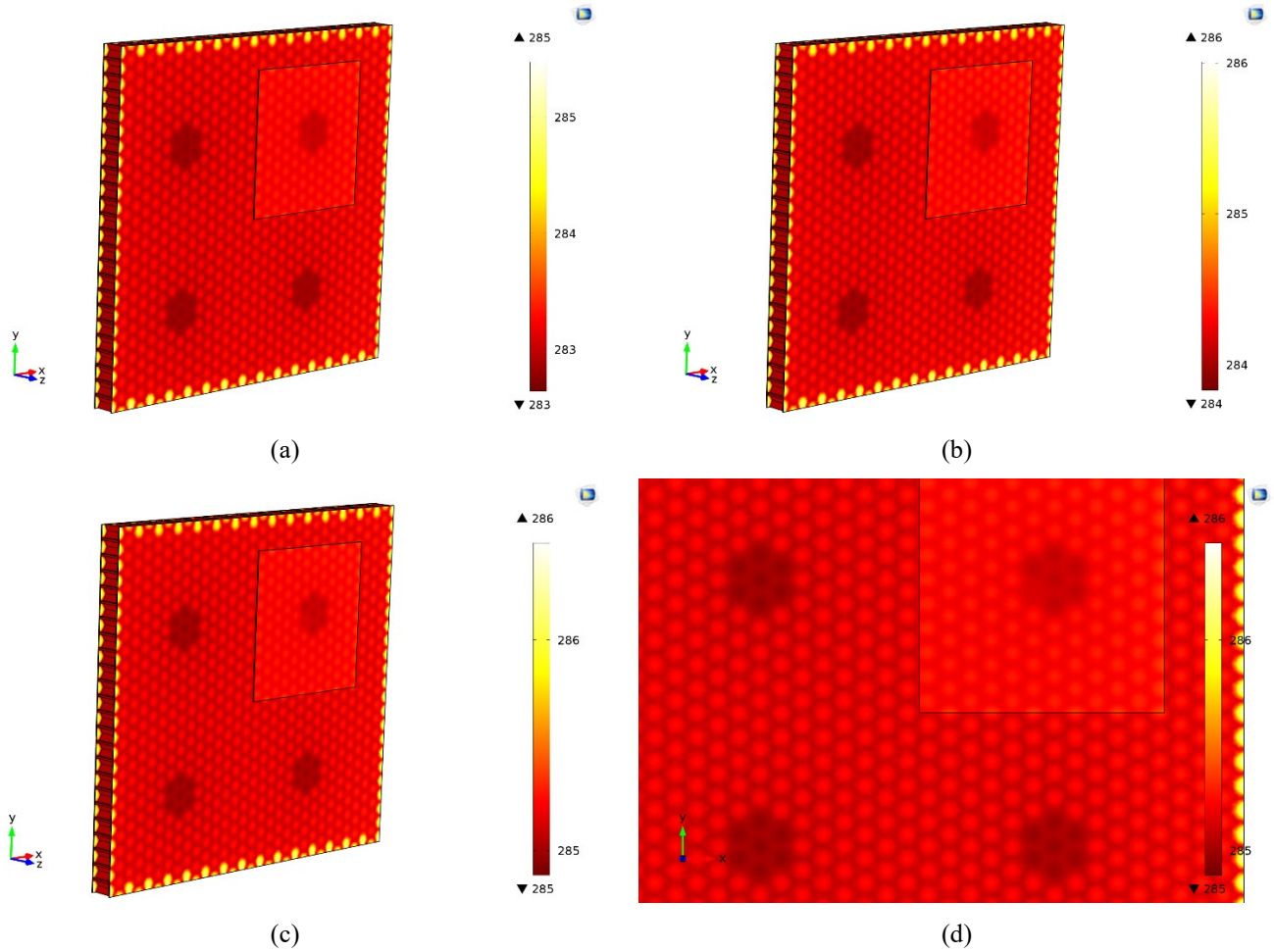

Fig. 11 – Trend of temperature field ranging from 20 /min to the end of the transition state: a) 20 /min, b) 30 /min, c) 40 /min, and d) expansion of the alveolar areas (at 40 /min) filled with water. The temperature is expressed in /K.

In addition, in Fig. 11 it is possible to evaluate how the passage of time involves a constant decrease of the temperature gradient between the various part of the specimen. Fig. 11 a) shows a temperature range of only 2 /K which remains the same in Fig. 11 b), although the minimum value increases by 1 /K. In Fig. 11 c), the maximum temperature remains unchanged with respect to Fig. 11 b), while the minimum temperature increases by 1 /K, making the gradient over the whole specimen of 1 /K.

By carefully observing the magnification of Fig. 11 d), it is possible to notice how the chromatic tone of the areas of interest is homogeneous less than the border areas of the sandwich panel. These parts, indeed, due to the tabs effect tend to be uniform to the temperature of the undisturbed environment. The thermal gradient calculated with a *Boundary Point Probe* estimated the maximum temperatures of the three-dimensional shells corresponding to the alveoli with a fluid at 285.069630437589 /K, and that corresponding to the alveoli at 285.2836386316655 /K without the presence of a fluid.

Then, by referring to the areas marked in Fig. 2 with §1, §2, §3 and §4, in Fig. 12a) it is possible to observe the comparison of the temperature trends obtained by means of the laboratory test and the simulated model.

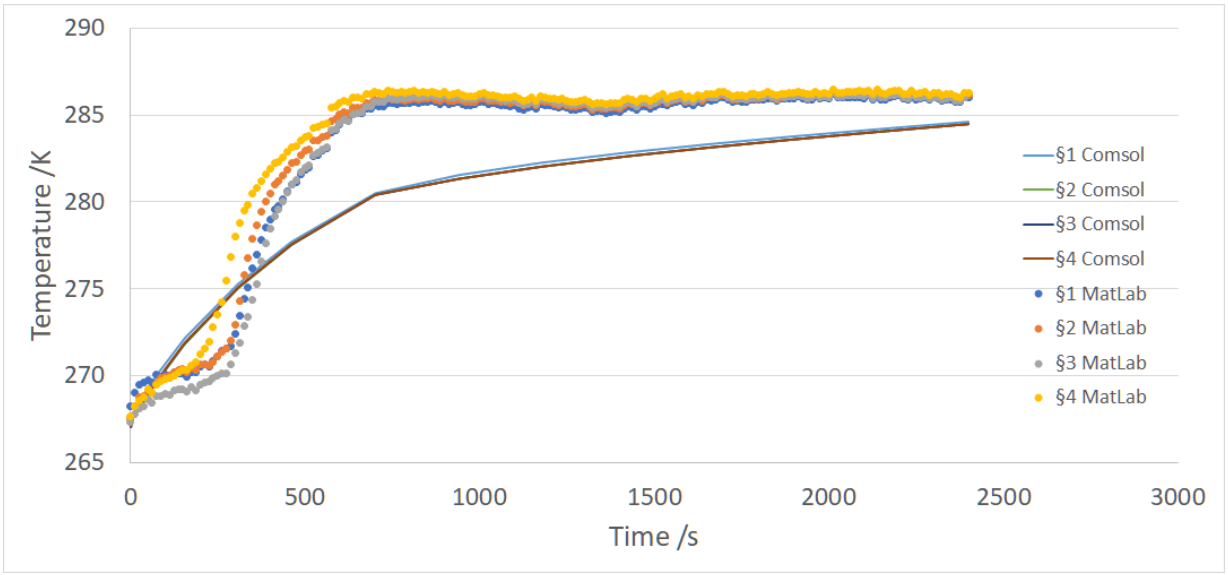

a)

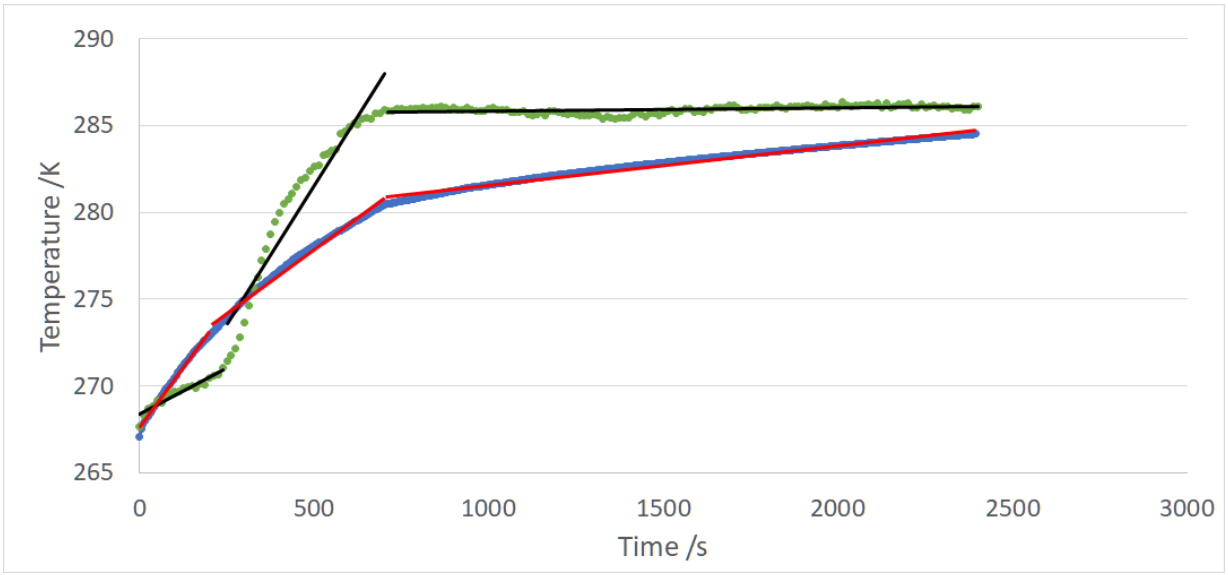

b)

Fig. 12 – a) Temperature field trends inherent to the zones marked by §1, §2, §3 and §4 (Fig. 2) both for the experimental test (MATLAB®) and the simulated model (Comsol®), and b) evidence of the regression curves evaluated on the average trends.

As above-mentioned, the temperature trend was obtained through an analysis of the thermograms performed in MATLAB® environment via a dedicated script. This occurred by averaging the temperatures of the alveolar areas filled with water (both in the state of solid aggregation and in the liquid aggregation, depending on the external thermal field induced on the specimen itself).

As regards the numerical model, a *Boundary Probe* was used for every interesting area, carefully to select the same area in reference to the real test. The temperature range in Fig. 12a) indicated by MATLAB® were obtained through the areas in Fig. 2. Also, in the legend of Fig. 12a), the name Comsol® indicates the simulated trend. In both cases, there is a very narrow band containing the temperature trends, both measured and simulated.

In particular, the four simulated curves are difficult to distinguish. Analysing the evolution of the thermal field for the thermographic test, it is clear that the surface temperature of the areas §3 and §4 is slightly lower than that of the zones §1 and §2. This is clearer until the first 250 /s, during which the temperature rises.

Given the vertical position of the specimen, the slight difference in temperature is attributable only to the absolute geodetic position of the defects due to both the fin effect (typical of thin thicknesses) and the local natural convection effects. No particular differences in thermal behaviour can be inferred even between §2 and §1, *i.e.*, where the detachment is located. The trend from 267 /K to 271 /K shows the latency of the aggregation state change. The trend from 271 /K to 285 /K shows a general heating up of the zones, that results to be very rapid depending on the thermal capacity of the composite hosting the alveoli filled with water. In the last phase, from about 700 /s to the end of the test, a temperature trend almost constant can be seen.

For the temperature trends of the numerical model, the same three trends described above are evident, although both the interval temperatures and the absolute values appear different. It is therefore possible to identify a latency of the state of aggregation from 267 /K to 272 /K, a general heating effect between 272 /K and 281 /K and, subsequently, a constant trend that leads to thermal equilibrium.

The affinities among the trend types are related to the derivative of the curves that, although showing a different angular coefficient, always maintains the same gradient of growth; this is evident in all areas and for all trends. To demonstrate this, in Fig. 12b) the trends obtained by MATLAB® and Comsol® are shown in green and blue, respectively, although in terms of average value between the curves o interest compared to those shown in Fig. 12a). The regression lines, in black and red colours, respectively, were linked to the trends. They were evaluated with respect to the main heating phases. These regression lines have, in this case, the sole purpose of highlighting the direction of the tangent to the simulated average trend. In Fig. 12b) it is evident that the regression curves (in black for the MATLAB® model, and in red for the Comsol® model) have a similar gradient behaviour for all the respective phases. Only the absolute values of the respective angular coefficients (per each phase) differ between them. The slight trend differences are typical of any

numerical simulation, even if accurate, both in terms of representation of the CAD model and the problem-solving algorithm applied.

Furthermore, the equilibrium of the temperature at the end of the test is similar because, as shown in Fig. 12a), there is a difference of less than 1 /K among the calculated and the modelled temperature.

The model, therefore, well approximates the calculation of the temperature of equilibrium.

Fig. 13 shows the trend of the measured and simulated temperatures inherent to a non-defective zone sufficiently distant from §1-4 (red dot marked in Fig. 7).

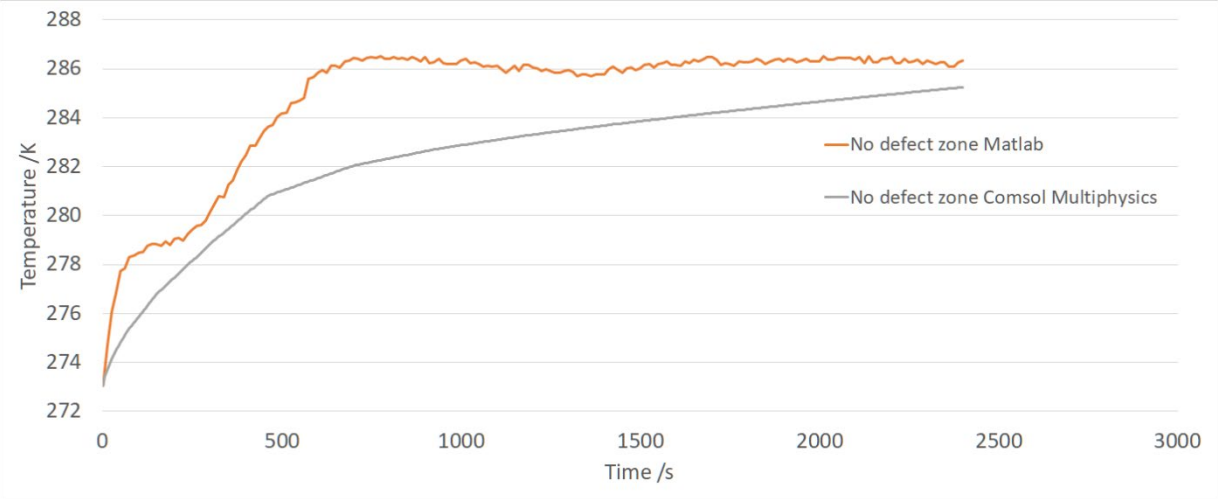

Fig. 13 – Trends of the temperature range for both the thermographic test and the numerical model, inherent to the area marked in Fig. 7.

As it is appreciable, since the alveoli are not filled with water in the state of solid aggregation, the thermal equilibrium of the specimen for the measured case appears very rapid in the first time instants of the test. From 278 /K to ~ 279 /K, an abrupt slowdown is shown. This behaviour is attributable to the influence of the surrounding area of the specimen surface, which is affected by the heat transmission effect due to the surrounding fluid (*i.e.*, the water).

It can be noted that, after this step, the specimen shows a rapid heating up to 286 /K, and then it continues with a constant trend along the thermal equilibrium phase. The same behaviour is also visible for the numerical model as the first derivative, that increase itself with the angular coefficient having a considerable slope, shows the same effect for the same time interval (*i.e.*, from 0 /s to ~100 /s).

A reduction of the gradient between ~100 /s and ~550 /s is also evident for the simulated trend. It then shows again a monotonous trend from ~550 /s to the end of the test.

The good agreement among the trends is clear, also in terms of the forecast of the final temperature to be reached at the equilibrium state. The slowdown effect to heating (as pointed out between ~100 /s and 600

/s) is also visible in Fig. 10 where, passing from Fig. 10 a) to Fig. 10 f), the alveoli below the skin appear less visible; this is indeed a symptom of temperature homogenization.

7. Analysis of the defects with Independent Component Thermography (ICT) technique

The thermograms were acquired in image format and, in order to proceed with the analysis, it was necessary to convert them into matrices. These matrices were ordered along a temporal acquisition sequence by building a tensor. The final tensor has two dimensions in terms of rows and columns coinciding with the pixels of the thermograms, while the third dimension consists of the matrices ordered according to the time instants of acquisition. After the construction of the tensor, data was processed through the Fast Independent Component Analysis (ICA) algorithm.

ICA is a statistical and computational technique for revealing hidden factors that underlie sets of random variables, measurements, or signals. ICA defines a generative model for the observed multivariate data, which is typically given as a large database of samples. In the model, the data variables are assumed to be linear mixtures of some unknown latent variables, and the mixing system is also unknown. The latent variables are assumed non-gaussian and mutually independent, and they are called the independent components of the observed data. These independent components, also called sources or factors, can be found by ICA. ICA is superficially related to principal component analysis (PCA) and factor analysis [51]. ICA is a much more powerful technique, however, capable of finding the underlying factors or sources when these classic methods fail completely.

In our case, the data analysed by ICA originate from digital images and the parameter of interest was the temperature, therefore, all the scalar values representing the elements constituting the single matrix (*i.e.*, every single pixel of the thermogram) were statistically estimated.

To simplify the understanding of the procedure, X and Y are the coordinates of an element of the matrix / thermogram, while Z is the coordinate that estimates the number of matrices / thermograms acquired over time. The procedure provides that each single element constituting the matrix in position X and Y (*i.e.*, each pixel of the thermogram) is estimated in the same position with respect to all the remaining matrices of the tensor Z, by ensuring that the comparison takes place only between the elements with fixed X and Y position, for all the values of Z. During the comparison, the algorithm looks for a law that expresses the single temperature parameter as a linear combination of the remaining ones. It is possible that some specific points of the single matrix / thermogram do not follow the law identified for the definition of the linear combination. In this case, these elements are called latent points. These points, because they are not a linear combination of the remaining ones, can be considered independent components.

The MATLAB® script shows by means of false colours the linearly dependent elements (in blue) and the independent components (in yellow) corresponding to the latent variables for each specific matrix / thermogram analysed. From this, the temporal instant is reconstructed; therefore, the specific defect becomes a latent variable. Following the analysis of all the matrices, a selection of time instants are shown in Fig. 14, for which the defective zones (in yellow) are considered the latent variables.

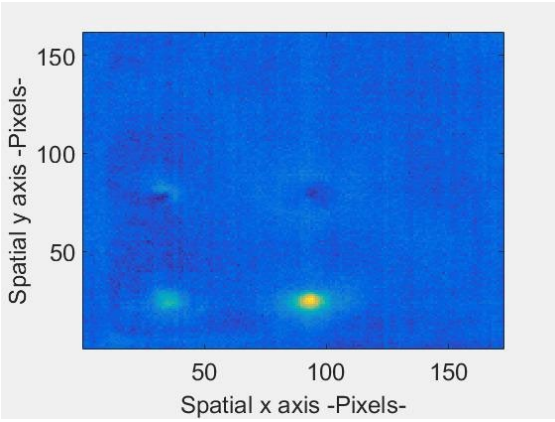

a)

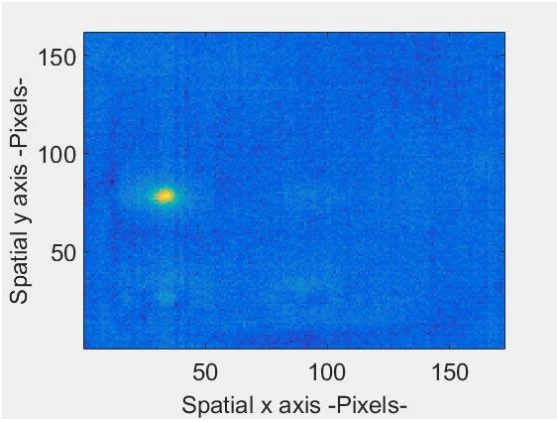

b)

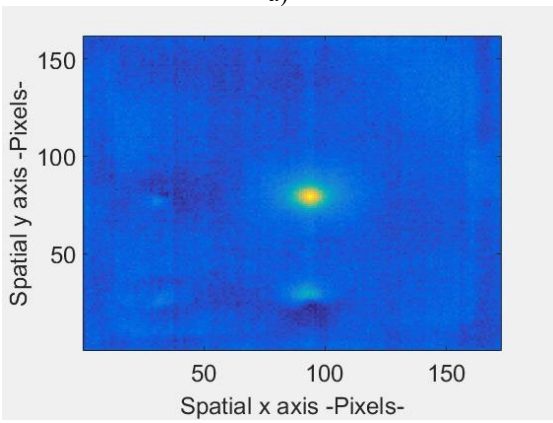

c)

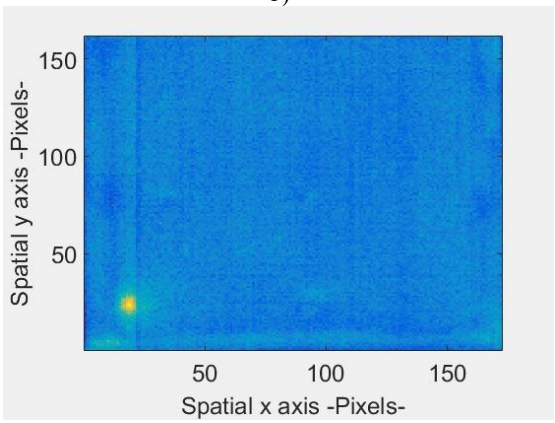

d)

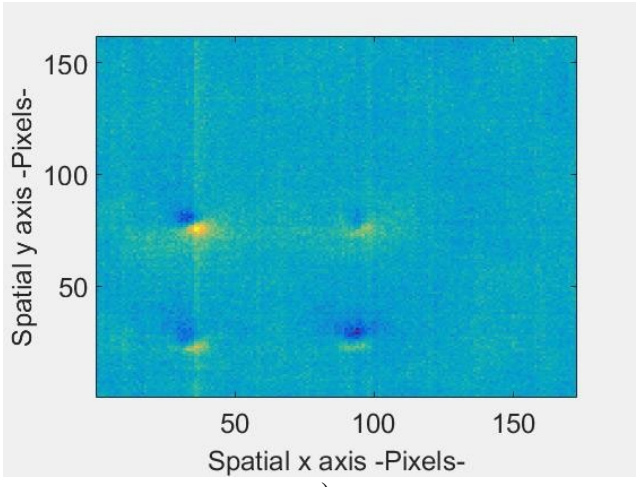

e)

Fig. 14 – Analysis with fast Independent Component Analysis (ICA) algorithm: a) trend reconstructed at thermogram 2 (time 20 /s), b) trend reconstructed at thermogram 5 (time 50 /s), c) trend reconstructed at thermogram 6 (time 60 /s), d) trend reconstructed at thermogram 9 (time 90 /s), and e) trend reconstructed at thermogram 12 (time 120 /s).

As can be seen from Fig. 14a), at just 20 /s of heating, the defects §3 and §4 are evident, in particular the latter one. Statistically, the temperature trend in the yellow areas is particularly distant with respect to the law identified as linear dependence. The areas §1 and §2 are also identifiable, but it is clear that their deviation towards a non-linearity trend is very moderate. Instead, in Fig. 14b), the area §1 is particularly evident. In Fig. 14c), the defect §2 is detectable, while the remaining areas (§1, §3, and §4) are barely visible.

In Fig. 14d), the area §3 is quite clear, but the peculiarity is the extension of the area in yellow. In fact, only the central part of the area §3 is largely interested to the non-linearity effect.

In Fig. 14e), all the §1, §2, §3, and §4 areas are obvious and not linear. This shows that only the centroid of such defects has a very different temperature compared to the whole specimen, which is very homogeneous in terms of temperature. Here, the §1, §2, §3, and §4 areas become evident due to the heating effect that affects the fluid inside the alveoli. At this stage, since the entire sample is closest to the thermal equilibrium between material and fluid, the individual behaviours of each area are less evident in favour of the global evidence of defects. In fact, it is possible to notice the the non-linearity effect is less extended and not well defined, although present on the four defects.

Fig. 15 shows the time instants for which the algorithm finds the greatest number of elements that cannot be represented as a linear combination between the matrices / temperatures.

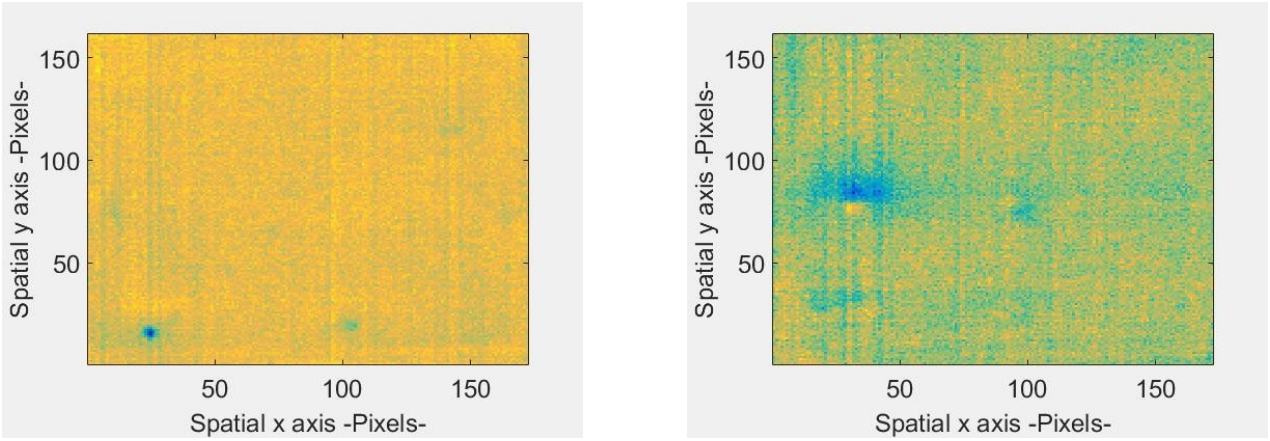

a) b)

Fig. 15 – Analysis with fast Independent Component Analysis (ICA) algorithm: a) trend reconstructed at thermogram 29 (time 290 /s), and b) trend reconstructed at thermogram 63 (time 630 /s).

In Fig. 15a it is possible to see how, except for §3 and §4, the remaining part of the specimen has a behaviour not linearly dependent with respect to the temperature parameter. This is attributable to the end of the change of state of aggregation from solid to liquid of the defective areas §1, §2, §3 and §4, with a re-adjustment of the temperature range for the whole specimen. As the heating continues, in Fig. 15b) it is possible to notice how the pattern in false colours shows a return to the linear dependence typical of the ending of the influence of the effect of the aggregation state change on the specimen itself. Here, the defective areas §1 and §2 that are tending to the blue colour are barely evident, even if they go towards a gradual homogenization.

Fig. 16 shows the time instant for which the algorithm detects the presence of the area §4, while for the remaining part of the specimen homogeneous and uniform heating is evident.

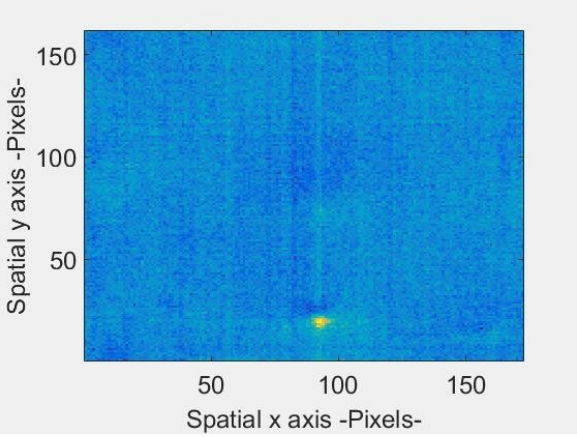

Fig. 16 – Analysis with fast Independent Component Analysis (ICA) algorithm: trend reconstructed at thermogram 53 (time 530 /s).

All the Figs. 14, 15 and 16 show the importance of the ICT technique, in that it is possible to note the presence of areas that may contain behavioural anomalies attributable to the detachment or inclusion of foreign material (*i.e.*, water). The peculiarity is due to the fact that the critical points are not highlighted only into a limited number of thermograms [52], but they are also evident in case the phenomenon of temperature variation seems to be less evident. This allows having a greater certainty of the defect analysis in samples under test since the technique is less affected to the punctual behaviour of a parameter, being instead in favour of a global estimate of the variables. For this reason, long-lasting thermographic campaigns allow an in-depth analysis of the possible presence of defects [53–56] inside a sandwich panel subjected to the water ingress phenomenon.

8. Conclusions

The evaluation of the freeze-thaw [57] phenomenon in sandwich-structured composites via numerical simulations and infrared thermography has been treated in this work.

In particular, the numerical model approximates the equilibrium temperature of the experimental test with a satisfying agreement. Also, for what concerns the prediction of the equilibrium time, the agreement among them is reasonable. This is evident from the oscillation of the temperature field which dies down in amplitude to the increase of the time for the curves measured at times greater than 1000 /s (Figs. 12a and 13).

The slight differences in behaviour between the temperatures estimated by the model in the phase of change of aggregation state may depend of many factors, *e.g.*, purity of the water, and volume of the fluid that during the phase of passage of state towards a liquid aggregation can leak from the holes drilled on the specimen surface. It is, however, believed that the numerical model is in agreement with the experimental trend.

The ICT technique demonstrated its ability to find defects caused by water ingresses. This is the first time, to the best of the authors' knowledge, that ICT technique was applied to detect such type of defect. Considering the very low quantity of water injected in every area (§1, §2, §3, §4) this can be considered an interesting result that opens the doors to further research inherent to injection of more dense fluids (*i.e.*, oil).

From a thermographic point-of-view, the lack of detection of the detached area may be attributed to the thermal stimulus applied, that is not suitable to generate a good thermal contrast on such type of defect (that is made up of a very thin layer of foreign material), as usually happens, instead, in the case of lamps [55–56]. By reducing the distance between the sample and the external lens of the thermal camera, a greater definition of the area of interest should be obtained, along with a reduction of thermal noise. In addition, the use of a double thermal camera which collect thermal images in parallel both from the front and the rear side of the sample when "immersed" into the climatic chamber will be explored in the second step of the present research. This, in order to have a sort of comparison in term of temperature variation with a reference area of the inspected sample. The fulfilment of the latter points can be considered a future perspective of the work.

9. Acknowledgments

Authors would like to thank Eng. E. Valentini from Mecaer Aviation Group (MAG), Monteprandone – Ascoli Piceno (AP), Italy, for providing the sandwich panel sample.

This work was financially supported by: UID/ECI/04708/2019- CONSTRUCT - Instituto de I&D em Estruturas e Construções funded by national funds through the FCT/MCTES (PIDDAC).

10. References

[1] https://pdfs.semanticscholar.org/bc00/402f3f47bbf9cab4dbb7d7f613d8c473f36e.pdf. Accessed 01 December 2019.

[2] https://apps.dtic.mil/dtic/tr/fulltext/u2/a402011.pdf. Accessed 01 December 2019.

[3] Geyer B. Drying method for composite honeycomb structures. In: Proceedings of the 28th International SAMPE Technical Conference, USA, November 1996, pp. 1183–1192.

[4] Anon. Airbus adopts infrared thermography for in-service inspection. Insight. 1994;**23**:774–5.

[5] Vavilov VP, Nesteruk DA. Detecting water in aviation honeycomb structures: the quantitative approach. Quant Infr Therm J. 2004;**1**:173–84.

[6] Vavilov V, Nesteruk D. Evaluating water content in aviation honeycomb panels by transient IR thermography. In: Proceedings of SPIE – The International Society for Optical Engineering – Thermosense XXVII, USA, March 2005, article number 55, 411–17.

[7] Crawley NM. Non-destructive testing & the link between environmental degradation & mechanical properties of composite honeycomb panels. In: Annual Forum Proceedings – AHS International 62nd Annual Forum, USA, May 2006, 1219–31.

[8] Tang BPY, Bennet LGI, Lewis WJ, Sweetapple CP, Francescone O. POD assessment of the RMC neutron radiology system for water detection in CF188 hornet flight control surfaces. In: 8th World Conference on Neutron Radiography (WCNR-8), USA, October 2006, 274–84.

[9] Lai WL, Kou SC, Poon CS, Tsang WF, Lai CC. Effects of elevated water temperatures on interfacial delaminations, failure modes and shear strength in externally-bonded CFRP-concrete beams using infrared thermography, gray-scale images and direct shear test. Constr Build Mater. 2009;**23**:3152–60.

[10] Sfarra S, Ibarra-Castanedo C, Avdelidis NP, Genest M, Bouchagier L, Kourousis D, Tsimogiannis A, Anastassopoulous A, Bendada A, Maldague X, Ambrosini D, Paoletti D. A comparative investigation for the non-destructive testing of honeycomb structures by holographic interferometry and infrared thermography. Journal of Physics: Conference Series. 2010;**214**:012071.

[11] Válek J, Kruschwitz S, Wőstmann J, Kind T, Valach J, Kőpp C, Lesák J. Nondestructive investigation of wet building material: multimethodical approach. J Perform Constr Fac. 2010;**24**:462–72.

[12] Zeng Z, Tao N, Feng L, Li Y, Zhang C. The effect of flash power on the measurement of thermal effusivity using thermal wave imaging. In: Proc. of SPIE – The International Society for Optical

Engineering – International Symposium on Photoelectronic Detection and Imaging 2011: Advances in Infrared Imaging and Applications, China, May 2011, article number 81930Y.

[13] Zeng Z, Tao N, Feng L, Li Y, Zhang C. Hidden heterogeneous materials recognition in pulsed thermography. AIP Conference Proceedings. 2012;**1430**:705–12.

[14] Guo X, Zhang F, Liu Y. Study on pulsed thermography for water ingress detection in composite honeycomb panels. Hangkong Xuebao/Acta Aeronautica et Astronautica Sinica. 2012;**33**:1134–46.

[15] Ibarra-Castanedo C, Brault L, Marcotte F, Genest M, Farley V, Maldague X. Water ingress detection in honeycomb sandwich panels by passive infrared thermography using a high-resolution thermal imaging camera. In: Proc. of SPIE – The International Society for Optical Engineering – Thermosense: Thermal Infrared Applications XXXIV, USA, April 2012, vol. 8354, article number 835405.

[16] Chen D, Zeng Z, Tao N, Zhang C, Zhang Z. Liquid ingress recognition in honeycomb structure by pulsed thermography. EPJ Applied Physics. 2013;**62**:120539.

[17] Chen D, Zeng Z, Zhang C, Jin X, Zhang Z. Quantitative study of water ingress in pulsed thermography. Insight. 2013;**55**:257–63.

[18] Avdelidis NP, Ibarra-Castanedo C, Maldague XPV. Infrared thermography inspection of glass reinforced plastic (GRP) wind turbine blades and the concept of an automated scanning device. In: Proc. of SPIE – The International Society for Optical Engineering – Thermosense: Thermal Infrared Applications XXXV, USA, April 2013, vol. 8705, article number 87050G.

[19] Martínez-Garrido MI, Gómez-Heras M, Fort R, Varas-Muriel MJ. Monitoring moisture distribution on stone and masonry walls. In: Rogerio-Candeleda M.A. (Ed.), Science, Technology and Cultural Heritage for the conservation of cultural heritage, CRC Press, Balkema, 2014, 35–40.

[20] Barreira E, Almeida RMSF, Delgado JMPQ. Infrared thermography for assessing moisture related phenomena in building components. Constr Build Mater. 2016;**110**:251–69.

[21] Adams J, Salvador M, Lucera L, Langner S, Spyropoulos GD, Fecher FW, Voigt MM, Dowland SA, Osvet A, Egelhaaf H-J, Brabec CJ. Water ingress in encapsulated inverted organic solar cells: correlating infrared imaging and photovoltaic performance. Adv Energy Mater. 2015;**5**:1501065.

[22] Saarimäki E, Laatikainen Y. Novel thermographic inspection method to detect the moisture in early stage of the water ingress and a procedure to remove the moisture from the composite

structure. In: 34th ICAF Conference and 28th Symposium of the International Committee on Aeronautical Fatigue and Structural Integrity (ICAF 2015), Finland, June 2015, vol. 2, 797–800.

[23] Isakov DV. Infrared detection of water ingress in a composite laminate crevice based on room temperature evaporation. Int J Heat Mass Tran. 2015;**86**:39–42.

[24] Vavilov V, Marinetti S, Pan Y, Chulkov A. Detecting water ingress in aviation honeycomb panels: qualitative and quantitative aspects. Polym Test. 2016;**54**:270–80.

[25] Chulkov AO, Vavilov VP, Moskovchenko AI, Pan Y-Y. Quantitative evaluation of water content in composite honeycomb structures by using one-sided IR thermography: is there any promise ?. In: Proc. of SPIE – The International Society for Optical Engineering – Thermosense: Thermal Infrared Applications XXXIX, USA, April 2017, vol. 10214, article number 102140U.

[26] Vavilov VP, Pan Y, Moskovchenko AI, Čapka A. Modelling detecting and evaluating water ingress in aviation honeycomb panels. Quant Infr Therm J. 2017;**14**:206–17.

[27] Bora M, Lordi V, Varley JB. Water ingress mapping in photovoltaic module packaging materials. In: IEEE 7th World Conference on Photovoltaic Energy Conversion (WCPEC 2018) – A joint Conference of 45th IEEE PVSC, 28th PVSEC and 34th EU PVSEC, USA, June 2018, code 143042.

[28] Duan Y, Liu S, Hu C, Hu J, Zhang H, Yan Y, Tao N, Zhang C, Maldague X, Fang Q, Ibarra-Castanedo C, Chen D, Li X, Meng J. Automated defect detection in infrared thermography based on a neural network. NDT&E Int. 2019;**107**:102147.

[29] Hu C, Duan Y, Liu S, Yan Y, Tao N, Osman A, Ibarra-Castanedo C, Sfarra S, Chen D, Zhang C. LSTM-RNN-based defect classification in honeycomb structures using infrared thermography. Infrared Phys Techn. 2019;**102**:103032.

[30] Shrestha R, Choi M, Kim W. Thermographic inspection of water ingress in composite honeycomb sandwich structure: a quantitative comparison among lock-in thermography algorithms. Quant Infr Therm J. 2019; DOI: 10.1080/17686733.2019.1697848.

[31] Yao Y, Sfarra S, Lagüela S, Ibarra-Castanedo C, Wu J.-Y, Maldague XPV, Ambrosini D. Active thermography testing and data analysis for the state of conservation of panel paintings. Int J Therm Sci. 2018;**126**:143–51.

[32] Liu Y, Wu J-Y, Liu K, Wen H-L, Yao Y, Sfarra S, Zhao C. Independent component thermography for non-destructive testing of defects in polymer composites. Meas Sci Technol. 2019;**30**:044006 (10 pp.).

[33] Zhang H, Sfarra S, Osman A, Szielasko K, Stumm C, Genest M, Maldague XPV. An infrared-induced terahertz imaging modality for foreign object detection in a lightweight honeycomb composite structure. IEEE T Ind Inform. 2018;**14**:5629–36.

[34] Zhang H, Sfarra S, Genest M, Ibarra-Castanedo C, Duan Y, Fernandes H, Avdelidis NP, Maldague XPV. A comparative study of enhanced infrared image processing for foreign object detection in lightweight composite honeycomb structures. Int J Thermophys. 2018;**39**:1–10.

[35] Ibarra-Castanedo C, Sfarra S, Ambrosini D, Paoletti D, Bendada A, Maldague X. Diagnostics of panel paintings using holographic interferometry and pulsed thermography. Quant Infr Therm J. 2010;**7**:85–114.

[36] Sfarra S, Theodorakeas P, Ibarra-Castanedo C, Avdelidis NP, Paoletti A, Paoletti D, Hrissagis K, Bendada A, Koui M, Maldague X. Evaluation of defects in panel paintings using infrared, optical and ultrasonic techniques. INSIGHT. 2012;**54**:21–7.

[37] http://www.tc.faa.gov/its/worldpac/techrpt/tc12-14.pdf. Accessed 01 December 2019.

[38] Sfarra S, Ibarra-Castanedo C, Theodorakeas P, Avdelidis NP, Perilli S, Zhang H, Nardi I, Koui M, Maldague XPV. Evaluation of the state of conservation of mosaics: simulations and thermographic signal processing. Int J Therm Sci. 2017;**117**:287–315.

[39] https://www.hexcel.com/user_area/content_media/raw/HexWeb_CRIII_DataSheet.pdf. Accessed 01 November 2019.

[40] http://www.matweb.com/search/datasheet_print.aspx?matguid=96d768abc51e4157a1b8f95856c49028. Accessed 01 November 2019.

[41] https://www.engineeringtoolbox.com/radiation-heat-emissivity-aluminum-d_433.html. Accessed 01 November 2019.

[42] https://www.azom.com/properties.aspx?ArticleID=764. Accessed 01 November 2019.

[43] https://www.thermoworks.com/emissivity-table. Accessed 01 November 2019.

[44] https://system.eu2.netsuite.com/core/media/media.nl?id=63786&c=3937524&h=a09b4bc563ba50c76da0&_xt=.pdf. Accessed 01 November 2019.

[45] Lin F, Bhatia GS, Ford JD. Thermal conductivities of powder-filled epoxy resins. J Appl Polym Sci. 1993;**49**:1901–08.

[46] Webster JG, Eren H. Measurement, Instrumentation, and Sensors Handbook: Two-Volume Set, 2nd edn. Boca Raton: CRC Press; 2014.

[47] http://usa.dupontteijinfilms.com/wp-content/uploads/2017/01/Mylar_Physical_Properties.pdf. Accessed 01 November 2019.

[48] https://www.engineeringtoolbox.com/water-html. Accessed 01 November 2019.

[49] https://www.engineeringtoolbox.com/ice-thermal-properties-d_576.html. Accessed 01 November 2019.

[50] Perilli S, Regi M, Sfarra S, Nardi I. Comparative analysis of heat transfer for an advanced composite material used as insulation in the building field by means of Comsol Multiphysics® and Matlab® computer programs. Rom J Mater. 2016;**46**:185–95.

[51] Lever J, Krzywinski M, Altman N. Principal Component Analysis. Nat Methods. 2017;**14**:641–2.

[52] Sfarra S, Ibarra-Castanedo C, Santulli C, Paoletti D, Maldague X. Monitoring of jute/hemp fiber hybrid laminates by non-destructive testing techniques. Sci Eng Compos Mater. 2016;**23**:283–300.

[53] Garrido I, Lagüela S, Sfarra S, Madruga FJ, Arias P. Automatic detection of moistures in different construction materials from thermographic images. J Therm Anal Calorim. 2019;**138**:1649–68.

[54] Sfarra S, Yao Y, Zhang H, Perilli S, Scozzafava M, Avdelidis NP, Maldague XPV. Precious walls built in indoor environments inspected numerically and experimentally within log-wave infrared (LWIR) and radio regions. J Therm Anal Calorim. 2019;**137**:1083–111.

[55] Yousefi B, Sfarra S, Ibarra-Castanedo C, Avdelidis NP, Maldague XPV. Thermography data fusion and nonnegative matrix factorization for the evaluation of cultural heritage objects and buildings. J Therm Anal Calorim. 2019;**136**:943–55.

[56] Yao Y, Sfarra S, Ibarra-Castanedo C, You R, Maldague XPV. The multi-dimensional ensemble empirical mode decomposition (MEEMD) – An advanced tool for thermographic diagnosis of mosaics. J Therm Anal Calorim. 2017;**128**:1841–58.

[57] Zhang X, Chen M, Huang Y. Isothermal drying kinetics of municipal sewage sludge coupled with additives and freeze-thaw preatreament. J Therm Anal Calorim. 2017;**128**:1195–1205.